Medical Engineering and Physics 67 (2019) 55–65

Contents lists available at ScienceDirect

Medical Engineering and Physics

journal homepage: www.elsevier.com/locate/medengphy

# Femur finite element model instantiation from partial anatomies using statistical shape and appearance models

Daniel Nolte*, Anthony M.J. Bull

*Department of Bioengineering, Imperial College London, London SW7 2AZ, United Kingdom*

ARTICLE INFO

*Article history:*
Received 24 July 2018
Revised 5 March 2019
Accepted 10 March 2019

*Keywords:*
Subject-specific modelling
Musculoskeletal simulation
Orthopaedic reconstruction
Anatomical measures

ABSTRACT

Accurate models of bone shapes are essential for orthopaedic reconstructions. The commonly used methods of using the contralateral side requires an intact bone and anatomical symmetry. Recent studies have shown that statistical shape and appearance models (SSAMs) as an alternative can predict accurate geometric models, but the accuracy of the mechanical property prediction is typically not addressed. This study compares stress and strain differences under identical loading conditions for reconstructions from partial anatomies.

SSAMs representing shape and grey values were created using 40 female cadaveric X-ray computed tomography scans. Finite element models were created for shape reconstructions from partial bone of various lengths with boundary conditions obtained from musculoskeletal simulations. Commonly used anatomical measures, measures of the surface deviations and maximal stresses and strains were used to compare the reconstruction accuracy to the contralateral side.

Surface errors were smaller compared to the contralateral side for reconstructions with 90% of the bone and slightly bigger when less bone was available. Anatomical measures were comparable. The contralateral side showed slightly smaller relative errors for strains of up to 6% on average.

This study has shown that SSAM reconstructions using partial bone geometry are a possible alternative to the contralateral side.



## 1. Introduction

Reconstructive orthopaedic surgery following complex trauma or to correct deformity requires the reconstructed shape, or target shape, to be known to enable custom devices such as cutting guides or implants to be created. The geometry of these devices and their surgical implantation accuracy can significantly affect functional outcome. For example, clinical studies have associated valgus aligned knee implants with an increased risk of ligament instability; and varus aligned knees with increased risk of tibial collapse [1], an altered joint range of motion [1,2] and increased risk of bone loss and cyst formation [3]. These findings have been confirmed in computational studies which have associated malaligned implants with increased wear [4,5], changes in joint kinematics such as problems with patella tracking and increased patellofemoral joint contact forces [6], and changes in the joint loading in the lower limb [7,8] which might lead to synovial pain, joint stiffness and an increased risk of osteoarthritis. Therefore, methods have been developed to reconstruct bone shape to a healthy, pre-trauma, or pre-deformity state.

A common method to reconstruct the healthy shape of a bone uses the contralateral side [9–11]. This approach requires an intact, healthy contralateral side and assumes symmetry. Although symmetry is shown for a number of variables [12,13], considerable differences between sides have been reported, especially in the long bones of healthy subjects [14–16]. Despite known asymmetries in patients who do not suffer from diagnosed conditions related to side discrepancies, patients presenting with bilateral trauma, severe osteoarthritis in the contralateral side or obvious deformities are not feasible to be treated using the contralateral side. Therefore, it is appropriate to consider alternative approaches for bone reconstruction.

Statistical shape models (SSMs) are widely used as an alternative to the approach using symmetry. Mauler et al. showed that shape predictions from SSMs of radius and ulna for the reconstruction of forearm bones from partial bones were able to predict the rotational axis with high accuracy, which enabled this approach to be used in correction osteotomies [17]. Plessers et al. [18] found

* Corresponding author.
*E-mail addresses:* d.nolte@imperial.ac.uk, daniel_nolte@gmx.de (D. Nolte), a.bull@imperial.ac.uk (A.M.J. Bull).

https://doi.org/10.1016/j.medengphy.2019.03.007
1350-4533/

that reconstructions from scapula shapes simulating glenoid defects using SSMs were able to predict the size and orientation of the glenoid accurately. Zhang and Besier investigated the accuracy of whole femur shape predictions from the proximal femur using SSMs and compared the predictions to linearly scaled models. They found that their predictions from SSMs had smaller overall shape errors and predicted the anatomical axis more accurately than linear scaling methods [19]. Schumann et al. [20] used SSM reconstructions to accurately predict the rotational alignment from the proximal and distal parts of fractured lower limb bones.

When designing implants for bone reconstruction, the mechanical properties are important as this enables stress shielding to be assessed, for example; stress shielding is seen in all types of joint replacement surgery [21,22]. Mechanical properties of bone will also affect fixation surgery and fixator design [23–25], which is important for deformity correction.

Few studies have combined the additional information required to estimate mechanical properties with SSMs. These studies typically referred to the models as statistical shape and appearance model (SSAM) or shape and intensity models (SSIM) and have been applied to generate: random new models of shape and density from the proximal part of a bone [26]; models for stress and strain analysis [27]; and to predict bone density of osteoporotic patients [28]. Zhang et al. developed an SSAM including the cortical thickness for femur bones [29]. There is no study that combines SSAMs to reconstruct partial bone shapes in three dimensions to enable mechanical analysis of the reconstruction surgery that might involve arthroplasty or limb realignment.

The aim of this study was to introduce methods to reconstruct the shape and mechanical properties of the femur from incomplete bone shapes using surface data alone and in combination with computed tomography (CT) grey value data using an SSAM. The methods were evaluated for use in pre-clinical testing of implant designs for massive bone reconstructions under realistic loading conditions. To evaluate the usability, the models were compared to the surrogate of the contralateral side. Commonly used anatomical measures allowing the congruence of the articulating surfaces and a correct anatomical alignment to be calculated were also quantified to evaluate the risk of malaligned lower limbs. These were: version angle, diaphysial-condylar angle, and varus/valgus alignment such as femoral neck angle, bow angle and the angle between the anatomical and mechanical axes.

## 2. Material and methods

### 2.1. Creation of SSAMs

CT scans (voxel size 1 mm × 0.8 mm × 0.8 mm) of 40 female cadaveric specimens (age 28–60 years, height 146 cm to 165 cm) taken from the Digital Korean (DK) dataset [30] were used to create SSAMs of the femur using a leave-one-out strategy. Surfaces of left and right femur were segmented and meshed with a maximal edge length of 2.25 mm using Mimics and 3-matics (Materialize, Belgium). SSAMs were created using a similar method as described in Bryan et al. [27] and surface models were registered following the method described in Nolte et al. [31]. In brief, the process consists of: selecting a reference shape by finding the bone with the median length; registering bone surfaces to the reference using an iterative closest point algorithm; establishing a point correspondence between surfaces by morphing the reference shape to each other shape using a non-rigid registration algorithm [32]; creating a tetrahedral mesh for the triangulated surface of the reference with a coarsening factor of 1.5 using Marc/Mentat (MSC Software Corporation, CA, USA) resulting in a mesh with 105,064 elements; transforming the mesh to match the surfaces of each subject by solving a Dirichlet boundary value problem as per Shontz and Vavasis [33]; and mapping Hounsfield units to the tetrahedral elements by assigning the value closest to the cell centre. Principal component analysis, implemented using a singular value decomposition of the covariance matrix of the surface point coordinates as described by Cootes and Taylor [34] was performed to calculate modes of variation.

### 2.2. Bone reconstruction

Defect models were created by cutting the segmented femur bones to retain the proximal 90%, 80%, 75% and 50% of the segmented femur bones (see Fig. 4(e)). Shapes were reconstructed from the SSAMs with a leave-one-out strategy using two methods. The first reconstructs the shape by minimising the root-mean-squared (RMS) deviation between surface points and closest point on the model surface (method surf). This method simulates the case where shape information, but not bone density information is available, such as for reconstructions from MRI or ultrasound images. The second method minimises a weighted average between surface distance and the root-mean-squared difference of grey values of model and grey value of the closest point in the nearest cell in the defect model (method surf-grey). This optimisation simulates the case for which CT images of the residual limb are available. Both methods iterate between minimising the distance by realigning the point set using an iterative closest point algorithm [35] and updating the coefficients of the modes of variation to adapt the shape model. Coefficients of the shape models were determined using a local constrained optimisation by linear approximation scheme [36].

The optimal number of modes of variation was determined prior to the reconstruction experiments using a randomly chosen sample bone and reconstructing the bone shape using gradually increasing numbers of modes. To minimise the effect of convergence to local solutions for the determination of the optimal number of modes, a global differential evaluation optimisation algorithm [37] was used. The number of modes of variations was increased until the deviation of the reconstructed bone to the source bone increased. This resulted in 25 modes of variation, which represented 87% of the accumulative variation of the SSAM. Calculating the reconstructions with the global optimisation resulted in up to 12% smaller RMS and Hausdorff distances (7% for 25 modes of variation) compared to the local optimisation, but since the runtime of the local optimisation was 99% faster than the global optimisation the local optimisation algorithm was used for the bulk of reconstructions in this study.

### 2.3. Comparison of morphological parameters

The accuracy of the geometric reconstruction was evaluated by measuring the overall deviation of the reconstructed bone surface compared to the reference shape segmented from CT images by calculating the RMS and the Hausdorff distance. These measures are important to evaluate the error which would add to the error of a potential implant manufacturing process. To evaluate the potential impact of deviations on the anatomy and the impact on kinematic changes of the subject, morphological parameters of the femur bones were evaluated using measures described in the literature [15,38,39]. These measures were as follows (after Dimitriou et al. [15]): the femoral head (FH) radius calculated by fitting a sphere to the FH, as per Dimitriou et al. [15]; the femoral neck angle between femoral anatomical axis (FAA) and the femoral neck axis (FNA), adapted from Dimitriou et al. [15]; bow angle between proximal and distal halves of the femoral shaft as implemented by Dimitriou et al. [15]; the angle between the FAA and the mechanical axis through the mid-point of the femoral epicondyles and

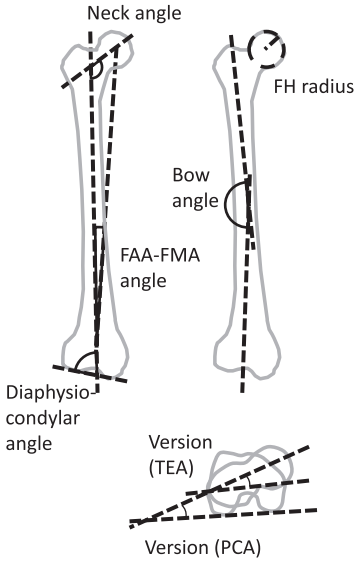


**Fig. 1.** Definition of anatomical measures: 3 dimensional angles were defined as femoral neck angle, angle between femoral anatomical and mechanical axis, bow angle and diaphyseal-condylar angle between distal condylar axis and femoral anatomical axis. Version (PCA) and (TEA) were calculated from projections of the neck axis and posterior condyle and trans-epicondylar axis, respectively, on to the transverse plane.

the FH centre as per Dimitriou et al. [15]; version angles between FNA and the axis through the posterior peaks of the femoral epicondyles (PCA) and between FNA and transepicondylar axis (TEA), projected on the transversal plane as implemented by Dimitriou et al. [15] and previously described by Murphy et al. [39]; and the diaphysial-condylar angle between FAA and the axis through the distal peaks of the epicondyles adapted from Kobyliansky et al. [38] (DCA; Fig. 1).

### 2.4. Calculation of joint loads using musculoskeletal simulations

To simulate the effect of complex loading conditions on tissue stresses and strains, boundary conditions for FE models were evaluated from the output of a musculoskeletal simulation. Medial and lateral tibiofemoral and patellofemoral joint contact forces as well as the centres of pressure were estimated from kinematics and ground reaction forces of a normal gait cycle measured for a sample subject using a validated musculoskeletal lower limb model (Freebody, [40,41]). The joint forces were transferred to the ISB femoral local coordinate system [42].

### 2.5. Finite element models

#### 2.5.1. Boundary conditions

The model was fixed at the femoral head through constraining nodes in all six degrees of freedom. Patellofemoral and medial and lateral tibiofemoral contact forces calculated from the musculoskeletal simulation were applied. These boundary conditions were applied over areas estimated at the hip, patellofemoral and tibiofemoral joint by projecting the joint centre for hip and knee, and medial and lateral tibiofemoral contact points along the force directions on to the surface. Areas were then determined by accumulating nodes within a radius of 4 mm of the projected point over all steps of the gait cycle. The resulting areas are shown in Fig. 2. Loads were spread equally to all nodes in the loading areas with force directions estimated from the musculoskeletal simulation.

#### 2.5.2. Material properties

A phantom-less calibration method was used to calibrate the CT scans [43]. Average grey values in ellipsoids with an area of 20 $mm^2$ identified as cortical bone, muscle tissue, fat and bone marrow were measured using Mimics (Materialize, Belgium) and were compared to calibrated values in the literature. The average Hounsfield units (HU) of 1548 ± 106, 18 ± 22, −87 ± 31 and −12 ± 36 for cortical bone, muscle, fat and bone marrow, respectively, matched the values presented as part of the software Bonemat ([44]; 1509, 90, −112, −17, respectively, Fig. 3).

Material properties were assigned to the elements by using the mapping procedure proposed in Schileo et al. [45] using the proposed relations between HU, radiological density $\rho_{QCT}$ in mg/$mm^3$, ash density $\rho_{ash}$ in mg/$mm^3$, apparent density $\rho_{app}$ in mg/$mm^3$, and Young's modulus $E$ in MPa:

$$\rho_{qct} = 0.0007964\,HU - 0.00393573$$

$$\rho_{ash} = \frac{\rho_{qct} + 0.09}{1.14}$$

$$\rho_{app} = 0.15 + 1.54\,\rho_{ash}$$

$$E = 8.920 \cdot 10^9\,\rho_{app}^{1.83}$$

This procedure included a mapping from quantitative CT density to ash density and from ash density to apparent density. For the mapping between bone apparent density (density in wet conditions) to Young's modulus the mixed relationship from Morgan et al. [46] was used. Following convergence analysis (described in 2.5.4), material properties were grouped into 150 discrete groups. A Poisson's ratio of 0.3 was used for all elements [44].

#### 2.5.3. Evaluation of results

The mechanical properties of the models were compared by evaluating the equivalent von Mises stress, equivalent elastic strain and displacement at five cross sections equally spaced at 60 mm increments starting 100 mm distal to the centre of the femoral head. This covered the distal part of the bone (Fig. 2). Maximal values of stresses, strains and displacements were evaluated at 49 sample points spaced on a regular lattice with a minimal distance of 3 mm between points. For each cross-section, maximal values were determined over all time steps and errors relative to the reference models were calculated.

#### 2.5.4. Convergence analysis

The number of material properties was determined by comparing stress and strain values for FE models of the SSAM mean shape using 1, 2, 5, 10, 20, 50, 100, 150 and 200 different materials, covering equal ranges of HU between 0 and 1800. Values outside this range were mapped to the closest value in this range. Convergence to less than 3% change was found for 150 material models, which was used in the remainder of the study.

Mesh convergence was tested using an FE model created from the mean shape of the SSAM created using surface meshes with maximal edge length of 3.0 mm, 2.25 mm and 1.5 mm resulting in tetrahedral meshes with 57,000, 105,000 and 242,000 elements by comparing stress, strain and displacement output. It was found that differences of less than 3% between models with 2.25 mm and 1.5 mm were assumed to be acceptable for this study.

### 2.6. Statistical analysis

Differences of RMS and Hausdorff distances, femoral head radius, femoral neck angle, bow angle, angle between femoral axes, version angles, diaphysial-condylar angle and angle between

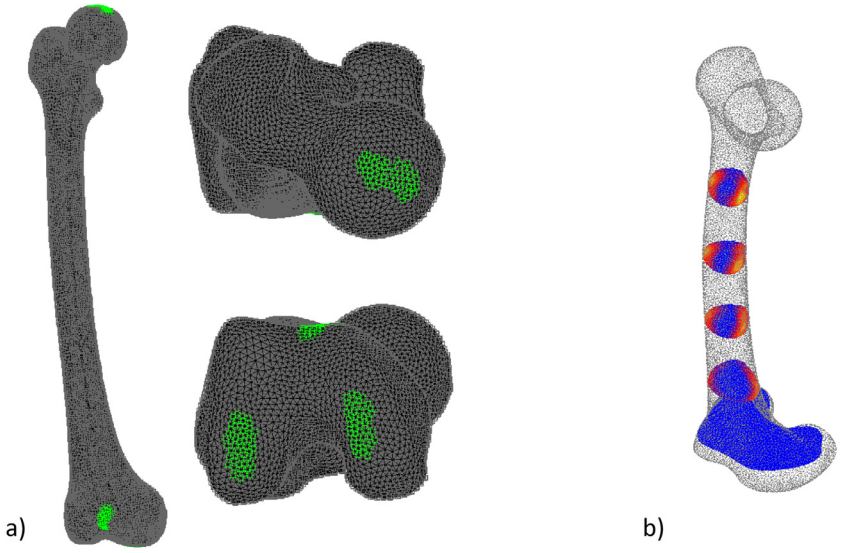


**Fig. 2.** Areas where boundary conditions are applied for medial and lateral tibiofemoral contact forces, patellofemoral contact forces and a fixation at the femoral head shown on one example geometry (a) and visualisation of planes for stress, strain and displacement measures used for comparison of the models (b).

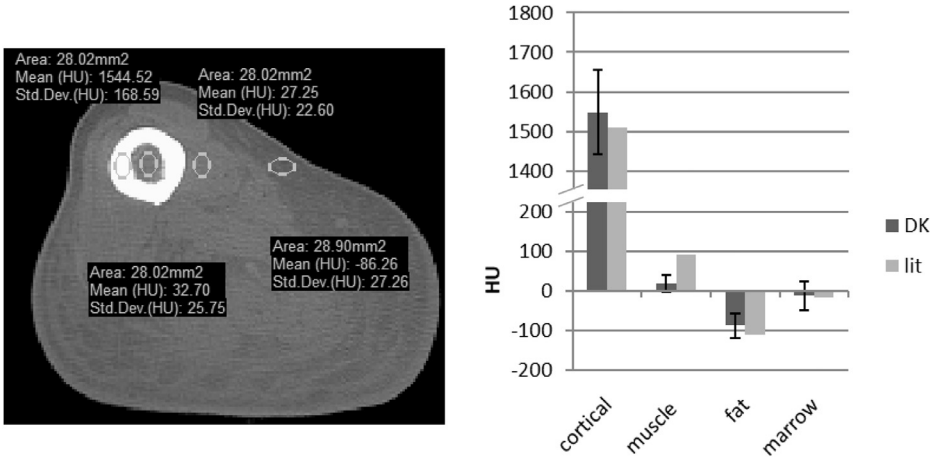


**Fig. 3.** Average Hounsfield units measured on 40 female subjects of the digital Korean (DK) dataset compared to Hounsfield units from a CT scan from the literature [44]. Error bars represent standard deviations.

condylar axes, relative errors of predicted maximal stresses, strains and displacements between reference and reconstructed or contralateral shape were tested. Shapiro–Wilk tests found that the data were not normally distributed. Therefore, Kruskal–Wallis tests with pairwise Wilcox signed-rank tests with Holm corrections for post-hoc analysis were performed. Statistical tests were performed for differences between reconstruction methods (surface measure vs surface and grey value measures vs contralateral) averaged over all defect models and for differences between defect levels (100–50% vs contralateral) averaged over the reconstruction methods as well as for each reconstruction method separately. All statistical tests were performed in R (R 3.4.3, www.r-project.org) using a significance value of $\alpha = 0.05$.

## 3. Results

The results are presented as follows, first the methods (surf vs surf-grey vs contralateral), and secondly, the different defect levels (contralateral vs 100–50%) are compared.

No statistical differences were found for the SSAM reconstruction using either the surface matching method or the surface and grey value matching method compared to the contralateral side averaged over the different defect models (Fig. 4). Nevertheless, differences for the shape reconstructions from the

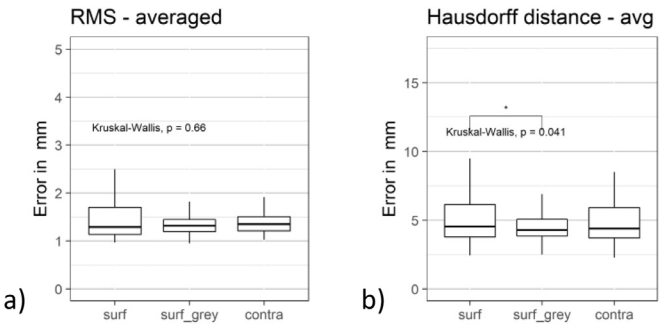


**Fig. 4.** Surface errors for all defect levels compared to the contralateral side of the surface and surface and grey value matching reconstruction methods averaged over all defect levels and the contralateral side measured as root mean square deviation (a) and Hausdorff distance (b) between surrogate and segmented bone surface. Statistically significant differences are marked using * ($p < 0.05$).

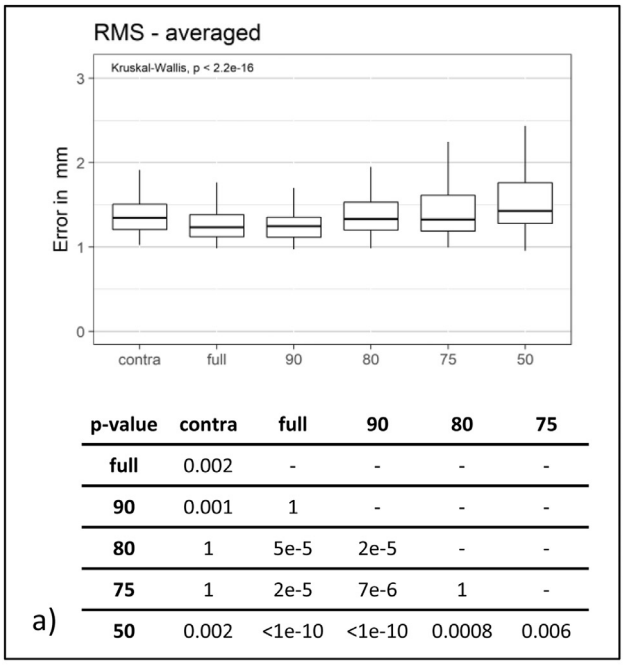


| p-value | contra | full | 90 | 80 | 75 |
|---|---|---|---|---|---|
| full | 0.002 | - | - | - | - |
| 90 | 0.001 | 1 | - | - | - |
| 80 | 1 | 5e-5 | 2e-5 | - | - |
| 75 | 1 | 2e-5 | 7e-6 | 1 | - |
| 50 | 0.002 | <1e-10 | <1e-10 | 0.0008 | 0.006 |

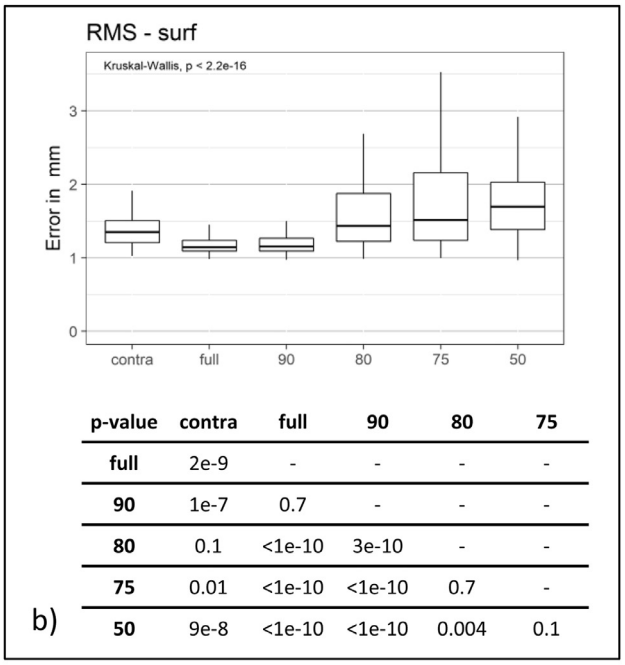


| p-value | contra | full | 90 | 80 | 75 |
|---|---|---|---|---|---|
| full | 2e-9 | - | - | - | - |
| 90 | 1e-7 | 0.7 | - | - | - |
| 80 | 0.1 | <1e-10 | 3e-10 | - | - |
| 75 | 0.01 | <1e-10 | <1e-10 | 0.7 | - |
| 50 | 9e-8 | <1e-10 | <1e-10 | 0.004 | 0.1 |

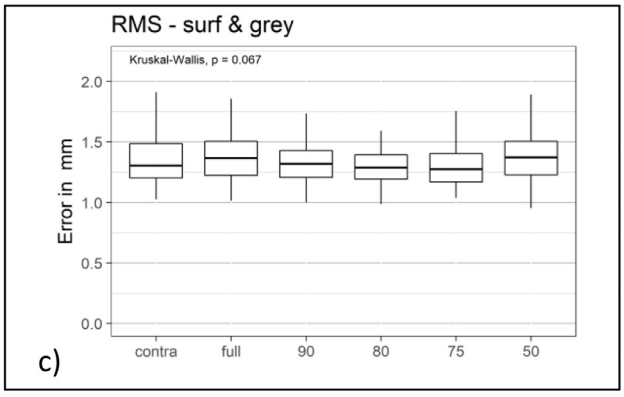


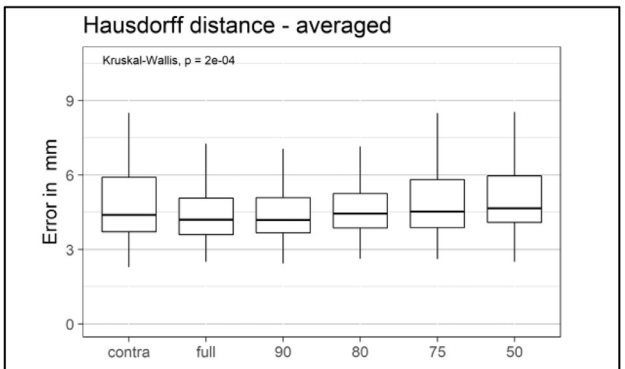


| p-value | contra | full | 90 | 80 | 75 |
|---|---|---|---|---|---|
| full | 0.9 | - | - | - | - |
| 90 | 1 | 1 | - | - | - |
| 80 | 1 | 0.07 | 0.1 | - | - |
| 75 | 1 | 0.03 | 0.5 | 1 | - |
| 50 | 0.09 | <1e-4 | <1e-4 | 0.1 | 0.5 |

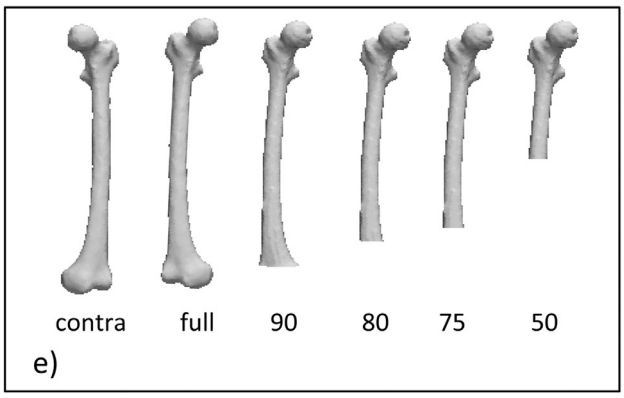


**Fig. 5.** Surface errors for all defect levels compared to the contralateral side measured as root mean square deviation for an average over both matching methods (a), for the surface matching method (b), for the surface and grey value matching method (c) and measured as Hausdorff distance averaged over both matching methods (d). *p*-values of pairwise comparisons are shown in the tables below the graphs. An illustration of the cutting planes and the residual bone is shown in (e).

full dataset and 90% of the points showed statistically significant lower RMS and Hausdorff deviations than reconstructions from the contralateral side for the surface matching method, whereas differences of reconstructions from 75% and 50% were statistically significant larger (Fig. 5). Average RMS errors tend to be smaller for reconstructions from larger defects for the surface and grey value matching, but these differences were not significant.

The average values and standard deviations of the anatomical measures are shown in Table 1, deviations from these measures are shown in Figs. 6 and 7. Significantly lower errors were found for the TEA version angles between the contralateral side and reconstructions from the full and 90% and 80% defect models as well as for all defect models for the PCA version angle (Fig. 7). For both version angle definitions both reconstruction methods deviations averaged over all defect models were significantly

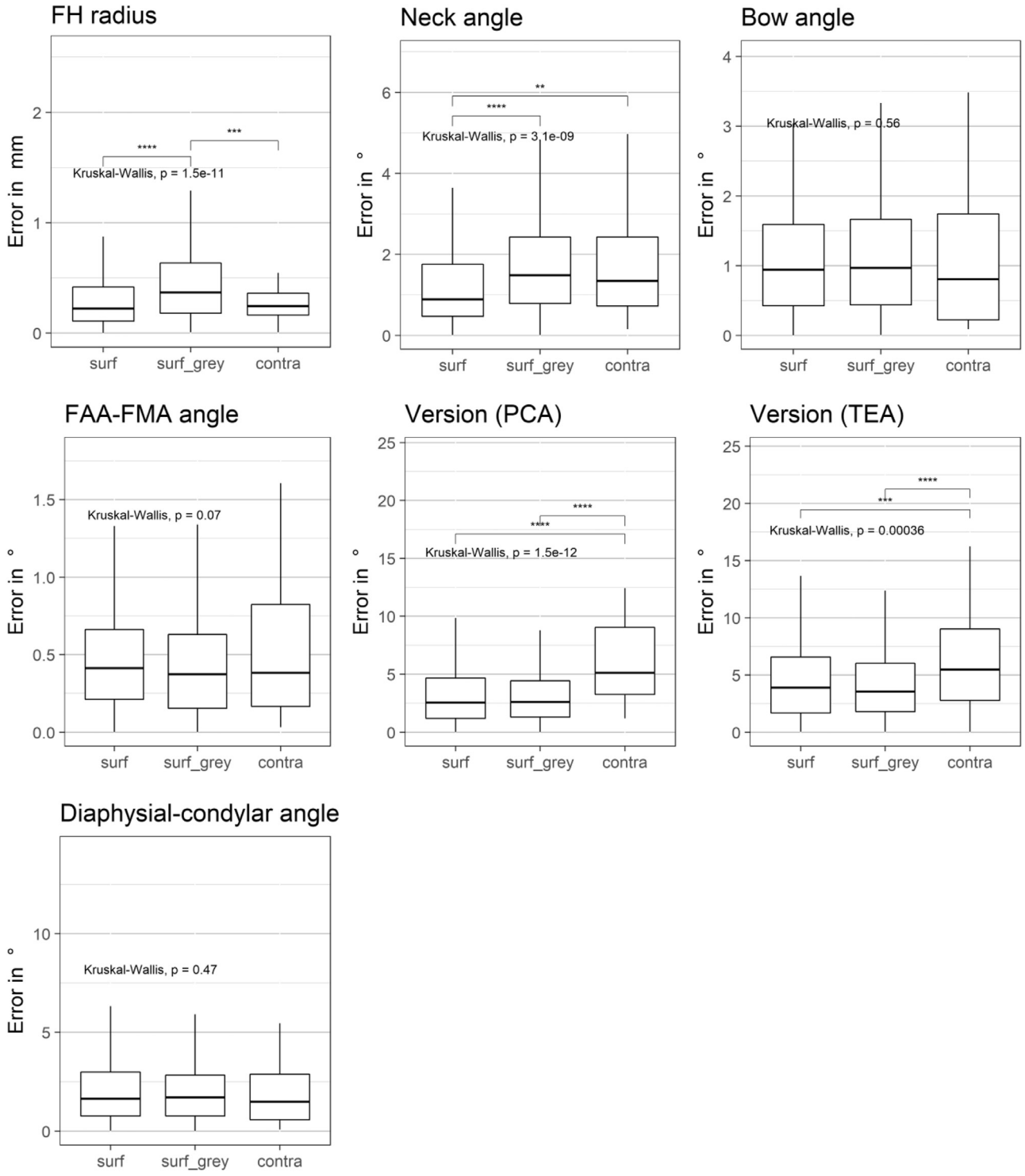


**Fig. 6.** Errors of femoral head (FH) radius, neck angle, bow angle, angle of femoral anatomical and mechanical axis, version angle defined using posterior condylar axis (PCA) and transepicondylar (TEA), and diaphysial-condylar angle for bone reconstructions for the two reconstruction methods averaged over all defect levels and the contralateral side. Statistically significant differences are marked using ** ($p < 0.01$), *** ($p < 0.001$) and **** ($p < 0.0001$).

smaller than for the contralateral side (Fig. 6). The prediction of the neck angle was statistically more accurate for the prediction using the surface measure compared to the contralateral side and the surface and grey value matching. The error of the femoral head radius was larger for the prediction using surface and grey value matching, but not for the surface matching procedure.

The differences in the mechanical analysis showed statistically significant lower maximal strains of the contralateral side compared to the SSAM reconstructed models and statistically significantly larger errors in distortion for the surface and grey value reconstructed models compared to the contralateral side, mainly due to larger errors for reconstructions from large defects. Errors in stresses were significantly smaller for surface reconstructed

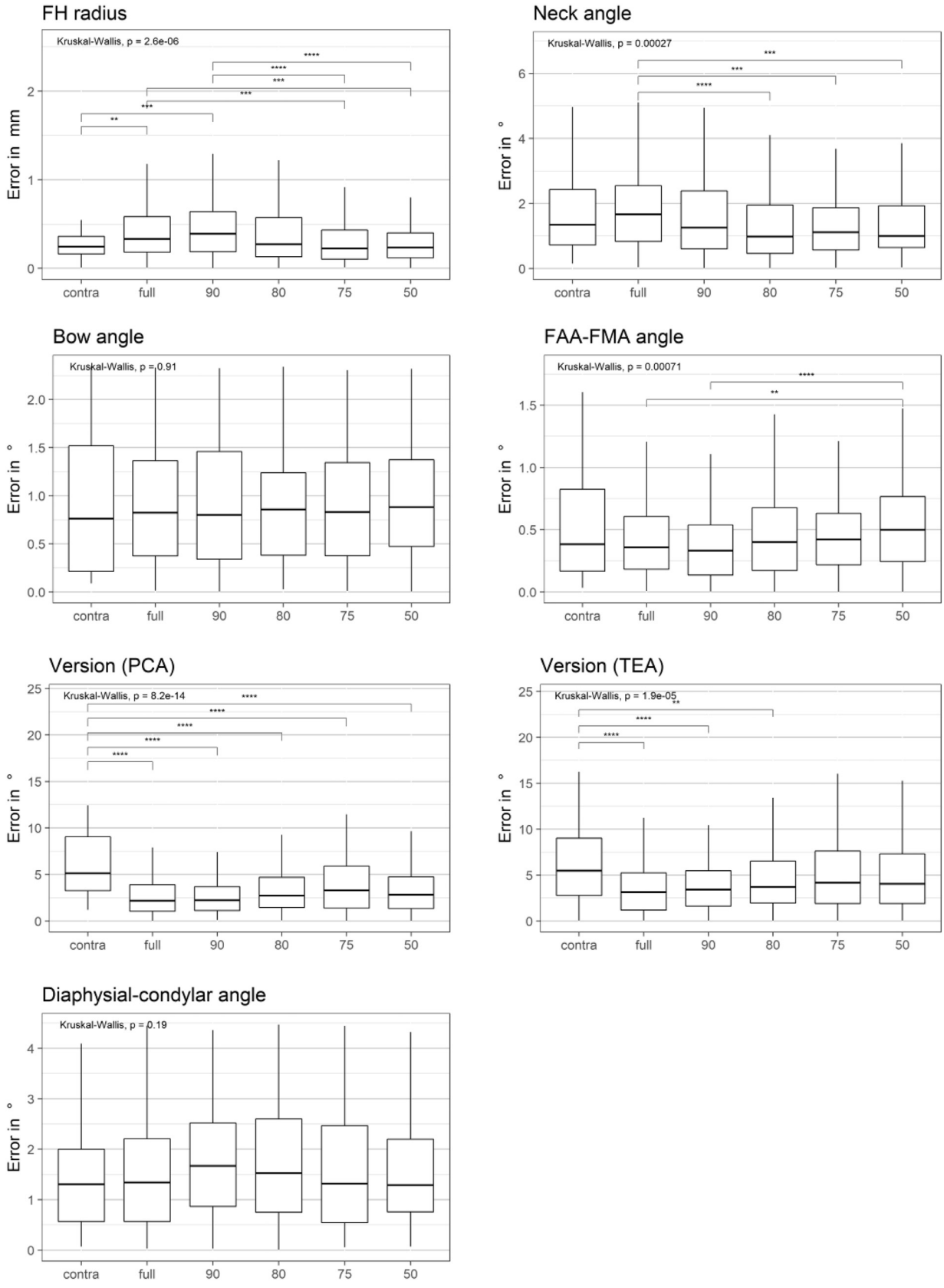


**Fig. 7.** Errors of femoral head (FH) radius, neck angle, bow angle, angle of femoral anatomical and mechanical axis, version angle defined using posterior condylar axis (PCA) and transepicondylar (TEA), and diaphysial-condylar angle for bone reconstructions for the different defect levels averaged over reconstruction methods and the contralateral side. Statistically significant differences are marked using ** ($p < 0.01$), *** ($p < 0.001$) and **** ($p < 0.0001$).

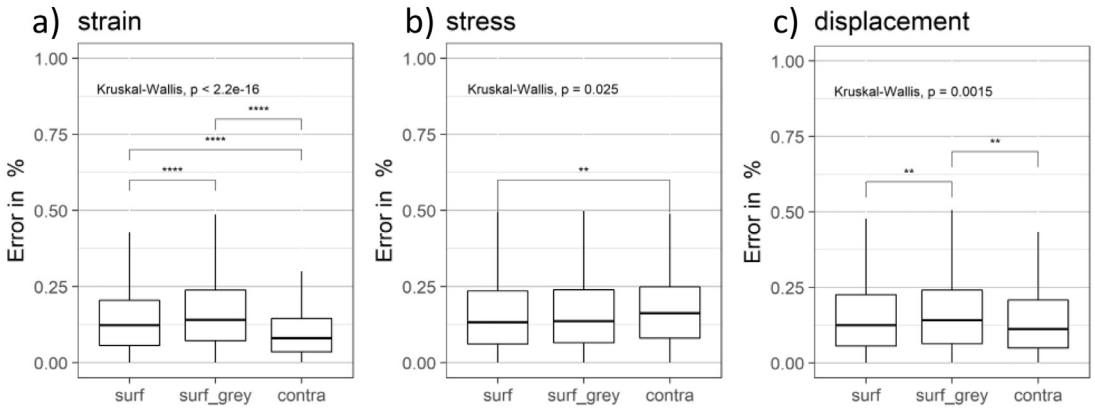


**Fig. 8.** Comparison of average relative errors in equivalent strain (a), von Mises stresses (b) and displacement (c) of both reconstruction methods averaged over all defect levels compared to the contralateral side. Statistically significant differences are marked using ** ($p < 0.01$) and **** ($p < 0.0001$).

**Table 1**
Values of anatomical measures derived from the SMMs and comparison with literature.

| | Reference average | Deviation contralateral side | Deviation full SSM reconstruction | Literature | Literature difference contralateral side |
|---|---|---|---|---|---|
| Femoral Head radius | 20.8 ± 1.0 mm | 0.3 ± 0.4 mm | 0.3 ± 0.4 mm | 22.3 ± 1.6 mm [15]<br>23 ± 2 mm [59] | 0.1 mm [15]<br>0 ± 2 mm [59] |
| Neck angle | 124.2 ± 4.0° | 1.7 ± 1.3° | 1.4 ± 1.3° | 126.7 ± 4.7° [15]<br>126.3 ± 5.5° [38] | 0.1° [15] |
| Femoral axis angle | 8.5 ± 0.8° | 0.5 ± 0.4° | 0.4 ± 0.2° | 6.8° [15] | 0° [15,16] |
| Bow angle | 171.4 ± 1.7° | 1.2 ± 1.0° | 1.0 ± 0.8° | 158.9 ± 6.1° [15] | 0° [15] |
| Version TEA | 21.2 ± 9.0° | 7.0 ± 5.7° | 2.4 ± 2.0° | 18.4 ± 8.5° [15]<br>20.9 ± 8.1° [38] | 1.4° [15] |
| Version PCA | 22.0 ± 8.7° | 7.2 ± 5.9° | 1.7 ± 1.4° | 12 ± 8.3° [15]<br>14.7°–16.4° [50] | 1.1° [15]<br>7° [16] |
| Diaphysial-condylar angle | 80.4 ± 3.3° | 0.5 ± 0.4° | 0.4 ± 0.2° | 81.9 ± 2.2° [38] | – |

surface compared to the contralateral side. Relative errors are shown in Figs. 8 and 9.

## 4. Discussion

In this study, algorithms to create a model of the shape and mechanical properties of the femur from surface landmarks and grey values obtained from a CT scan of an incomplete bone shape for the purpose of designing and testing implants for customised orthopaedic reconstructions were presented. SSAM representing the shape and bone mineral density in form of grey values of CT scans were constructed and bone shapes were reconstructed from landmarks representing different levels of bone defects. Whereas in clinical practice the input for the reconstruction using surface and grey value information requires using medical imaging using CT scans or biplanar X-rays, reconstructions using only surface landmarks can be achieved using magnet resonance or 3-dimensional ultrasound images [47,48].

The comparison of surface measures showed that shape reconstructions using SSAMs where only small regions (<20%) of the bone were excluded due to defects were more accurate than predictions using the contralateral side. The accuracy dropped for defect levels of more than 20%, which is approximately at the level of the metaphysis with the distal the growth plate which is assumed to be a region where the shape of the bone can be influenced by the loading during the growth phase and therefore allows for larger individual variations [49]. Nevertheless, reconstructions from only 50% of the bone had RMS and Hausdorff distances on average 0.7 mm and 2.5 mm larger, respectively, than the errors of the contralateral side, which is 2.5 times the resolution of the scans used to obtain the underlying data. These errors are comparable to errors reported a previous study for reconstructions of 50% of the bone [19].

The anatomical measures in this study were comparable to values in the literature (Table 1) where differences might be the result of differences in measuring the anatomical axis. Differences might also result from differences of gender and ethnicity reported in the different studies [50]. The SSAM reconstructions from more than 80% of the bone showed statistically significant lower errors of on average more than 3° for the prediction of the version angle compared to the contralateral side, when using the TEA and the PCA. Reconstructions using 80% or less did not show any significant differences to the contralateral side. Changes in the version angle are associated with an increased risk of fractures due to a change of loads in the proximal femur, an increased risk of acetabular labral injuries [51], and are correlated with knee OA prevalence [52]. Both studies give thresholds of more than 15° for an increased risk of OA. Therefore, the errors obtained in this study of, on average, less than 7° are not clinically significant. Statistically significant differences were found for the femoral head radius and the angle between the anatomical and mechanical axes. The difference in errors of the femoral head radius for reconstructions from smaller portions of the femur can be explained by a better fit of the proximal part of the bone. Since this study is focussing on models for the reconstruction of the distal femur, errors of less than 0.5 mm can be assumed as negligible. The errors in the femoral axis angle were below 0.7°. The difference of this angle results in a medial or lateral shift of the knee and therefore a change in varus or valgus alignment, which could also be caused by a change in the length of the bone [53]. Burghardt et al. found in their study that a change of less than 1° did not have any clinical effect [53]. According to these findings, the differences found in this study are not clinical significant.

The reconstructions in this study were performed with a local optimisation algorithm even though reconstructions of a sample shape showed that a global optimisation resulted in up to 7% lower

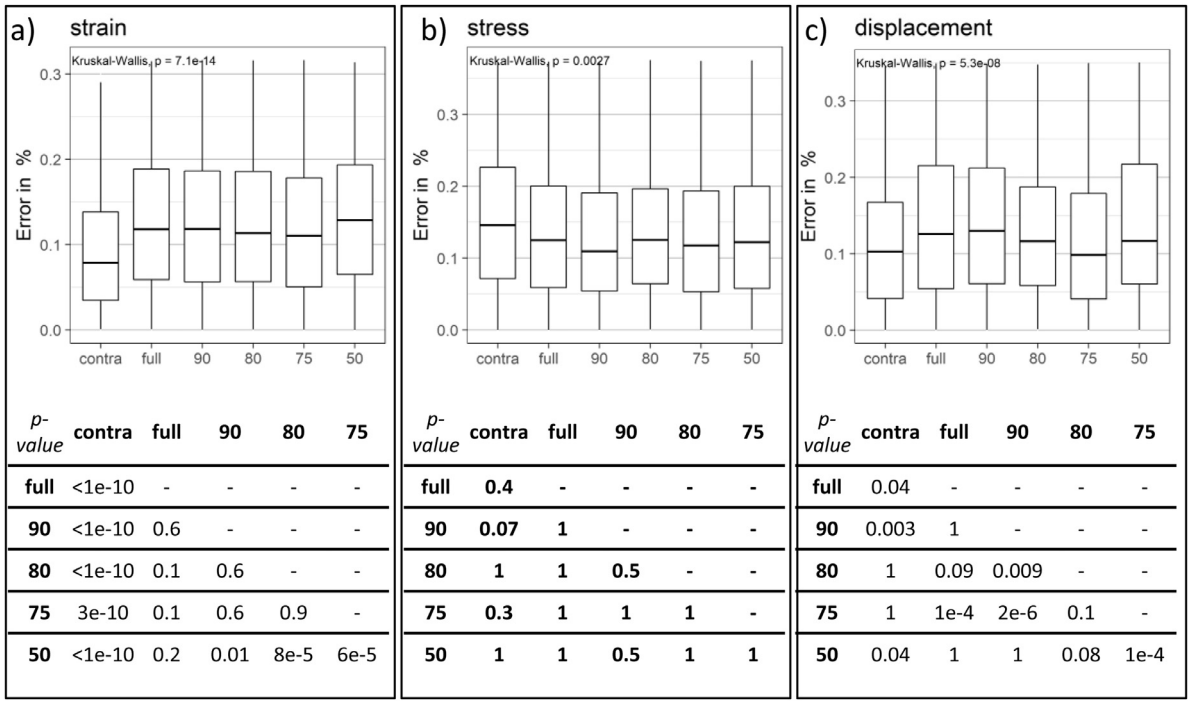


| *p-value* | contra | full | 90 | 80 | 75 |
|---|---|---|---|---|---|
| **full** | <1e-10 | - | - | - | - |
| **90** | <1e-10 | 0.6 | - | - | - |
| **80** | <1e-10 | 0.1 | 0.6 | - | - |
| **75** | 3e-10 | 0.1 | 0.6 | 0.9 | - |
| **50** | <1e-10 | 0.2 | 0.01 | 8e-5 | 6e-5 |

| *p-value* | contra | full | 90 | 80 | 75 |
|---|---|---|---|---|---|
| **full** | **0.4** | - | - | - | - |
| **90** | **0.07** | **1** | - | - | - |
| **80** | **1** | **1** | **0.5** | - | - |
| **75** | **0.3** | **1** | **1** | **1** | - |
| **50** | **1** | **1** | **0.5** | **1** | **1** |

| *p-value* | contra | full | 90 | 80 | 75 |
|---|---|---|---|---|---|
| **full** | 0.04 | - | - | - | - |
| **90** | 0.003 | 1 | - | - | - |
| **80** | 1 | 0.09 | 0.009 | - | - |
| **75** | 1 | 1e-4 | 2e-6 | 0.1 | - |
| **50** | 0.04 | 1 | 1 | 0.08 | 1e-4 |

**Fig. 9.** Comparison of average relative errors in equivalent strain (a), von Mises stresses (b) and displacement (c) between reconstructions from different defect levels averaged over both reconstruction methods and the contralateral side estimated. The *p*-values of pairwise comparisons are shown in the tables below the graphs.

errors. This shows that there might be some potential to further improve the results of the reconstruction. Due to a significantly higher runtime for the global optimisation, this algorithm was not used in this study.

Apart from predicting the shape, the SSAM reconstructions were also used to predict the mineral density inside the volume. The accuracy of these reconstructions were evaluated by using an FE analysis to compare stresses, strains and displacements under clinically relevant loading conditions as they could be used in pre-clinical FE testing of implants. This has not been attempted before. These loading conditions were derived from the musculoskeletal simulations of a gait cycle. In this study these boundary conditions were limited to the joint contact forces at the knee and hip, where previous studies have shown that muscle forces influence stresses and strains in the bone [54,55]. Therefore, neglecting these forces is a limitation of this study, although it is assumed that these additional forces would not change the differences between the models significantly and this study was focused on assessing these differences only, not on identified absolute values.

The comparison between the reconstruction methods did not show statistically significant differences for the relative errors of deformations and von Mises stresses between the SSAM reconstructions and the contralateral side with relative errors on average between 10% and 18%. Statistically significant differences were found for the strain measures which were on average 8% for the contralateral side and between 10% and 15% for the SSAM reconstruction, which arose from differences in the prediction of material properties. Since the material properties are derived only from the relationship between geometry and material properties represented in the SSAM, the prediction from the contralateral side might have the advantage of experiencing a similar level of loading as the reconstructed bone which results in a largely similar overall bone strength. Including additional information about the bone density of the unaffected part of a traumatic bone, as far as these can be obtained from medical images, might result in a lower prediction error for the mineral density. For the purpose of pre-clinical testing of implants, these errors might be acceptable considering the large difference of material properties of currently used implant materials [56]. Future work could aim to improve the accuracy of the material properties predictions by incorporating information about the tissue density in the affected bone according to the methodology implemented by Väänänen et al. [57]. A limitation of this study is the use of uncalibrated CT scans. To overcome the lack of calibration data, a phantom-less calibration method was used to quantify differences in calibration data of the images and compare to calibration data from the literature. This limits the results for the clinical use, but should give an indication about the accuracy of the presented methodology. For the mapping of the grey values from CT images to the FE models a closest voxel mapping was used. This method is prone to errors if the element size of the FE mesh is significantly different from the voxel size, in which case more elaborate methods like integration over contained voxels [44] could be used. Nevertheless, the convergence analysis performed in this study showed that a change in element size in this study had only small effects on the results.

The definition of a critical size for bone reconstruction has to consider several different factors, such as size of the bone loss, the state of the covering soft tissue, vascularity and the state of the neural system [58]. The simulated case of a 50% defect including the distal articulated surface might represent a critical defect size where, depending on the state of the surrounding tissue, an amputation is likely. On the other hand, a reconstruction from the 10% defect model represents the cases where the articulating surface is damaged or missing, but there is likely to be only a partial epiphysis damage such as might be the case for some knee arthroplasty surgeries. This study shows that in these cases using reconstruction from SSAMs are at least as accurate as using the contralateral side. Large defects (25% or more) are less accurate compared to the contralateral side and therefore the contralateral side would be the first choice. Nevertheless, if the contralateral side is not available as a template model, the SSAM reconstruction might still be reasonably accurate to be used for reconstructions.

In summary, this study showed that SSAMs as an alternative to shape reconstructions from the contralateral side are able to produce comparable accuracies for the bone shape. The predictions of material properties reconstructed only from the geometry showed errors that were slightly larger than predictions from the contralateral side, but which can be seen as a possible alternative in cases where the contralateral side is not available, material properties cannot be estimated due to a lack of CT imaging, or in cases where the patient should not be exposed to additional ionising radiation.

## Conflict of interest

The authors do not have any financial or personal relationships with other people or organisation that could inappropriately influence their work.

## Ethical approval

Not required.

## Acknowledgments

This work was supported by an EPSRC Global Research Fund (EP/P510798/1) and an NIHR Global Health Research Grant (GHR Project: 16/137/45). DN was supported by a Beit Fellowship for Scientific Research. The research is using data from the Digital Korean provided by the Korea Institute of Science and Technology Information.

## References

[1] Fang DM, Ritter MA, Davis KE. Coronal alignment in total knee arthroplasty. Just how important is it? J Arthroplasty 2009;24:39–43. doi:10.1016/j.arth.2009.04.034.
[2] Kaipel M, Gergely I, Sinz K, Neumann C, Sinz G. Femoral rotation in ligament balanced knee arthroplasty: a prospective clinical study. J Arthroplasty 2013;28:1103–6. doi:10.1016/j.arth.2013.02.031.
[3] Nielsen FK, Egund N, Jørgensen A, Jurik AG. Risk factors for joint replacement in knee osteoarthritis; a 15-year follow-up study. BMC Musculoskelet Disord 2017;18:510. doi:10.1186/s12891-017-1871-z.
[4] Suh D-S, Kang K-T, Son J, Kwon O-R, Baek C, Koh Y-G. Computational study on the effect of malalignment of the tibial component on the biomechanics of total knee arthroplasty. Bone Jt Res 2017;6:623–30. doi:10.1302/2046-3758.611.BJR-2016-0088.R2.
[5] Kang K-T, Koh Y-G, Son J, Kwon O-R, Baek C, Jung SH, et al. Measuring the effect of femoral malrotation on knee joint biomechanics for total knee arthroplasty using computational simulation. Bone Jt Res 2016;5:552–9. doi:10.1302/2046-3758.511.BJR-2016-0107.R1.
[6] Heyse TJ, El-Zayat BF, de Corte R, Chevalier Y, Fuchs-Winkelmann S, Labey L. Internal femoral component malrotation in TKA significantly alters tibiofemoral kinematics. Knee Surgery. Sport Traumatol Arthrosc 2017;0:1–9. doi:10.1007/s00167-017-4778-1.
[7] Lerner ZF, DeMers MS, Delp SL, Browning RC. How tibiofemoral alignment and contact locations affect predictions of medial and lateral tibiofemoral contact forces. J Biomech 2015;48:644–50. doi:10.1016/j.jbiomech.2014.12.049.
[8] Chen Z, Wang L, Liu Y, He J, Lian Q, Li D, et al. Effect of component malrotation on knee loading in total knee arthroplasty using multi-body dynamics modeling under a simulated walking gait. J Orthop Res 2015;33:1287–96. doi:10.1002/jor.22908.
[9] Hu L, Zhang J, Li C, Wang Y, Yang Y, Tang P, et al. A femur fracture reduction method based on anatomy of the contralateral side. Comput Biol Med 2013;43:840–6. doi:10.1016/j.compbiomed.2013.04.009.
[10] Qiu L, Zhang Y, Zhang Q, Xu L, Niu X, Zhang L. Allograft selection for distal femur through cutting contour registration. Cell Tissue Bank 2016;17:699–711. doi:10.1007/s10561-016-9580-7.
[11] Zhang W, Ji Y, Wang X, Liu J, Li D. Can the recovery of lower limb fractures be achieved by use of 3D printing mirror model? Injury 2017;48:2485–95. doi:10.1016/j.injury.2017.09.003.
[12] Young EY, Gebhart J, Cooperman D, Ahn NU. Are the left and right proximal femurs symmetric? Basic research.. Clin Orthop Relat Res 2013;471:1593–601. doi:10.1007/s11999-012-2704-x.
[13] Pierre MA, Zurakowski D, Nazarian A, Hauser-Kara DA, Snyder BD. Assessment of the bilateral asymmetry of human femurs based on physical, densitometric, and structural rigidity characteristics. J Biomech 2010;43:2228–36. doi:10.1016/j.jbiomech.2010.02.032.
[14] Auerbach BM, Ruff CB. Limb bone bilateral asymmetry: variability and commonality among modern humans. J Hum Evol 2006;50:203–18. doi:10.1016/j.jhevol.2005.09.004.
[15] Dimitriou D, Tsai TY, Yue B, Rubash HE, Kwon YM, Li G. Side-to-side variation in normal femoral morphology: 3D CT analysis of 122 femurs. Orthop Traumatol Surg Res 2016;102:91–7. doi:10.1016/j.otsr.2015.11.004.
[16] Eckhoff DG, Jacofsky DJ, Springer BD, Dunbar M, Cherian JJ, Elmallah RK, et al. Bilateral symmetrical comparison of femoral and Tibial anatomic features. J Arthroplasty 2016;31:1083–90. doi:10.1016/j.arth.2015.11.021.
[17] Mauler F, Langguth C, Schweizer A, Vlachopoulos L, Gass T, Lüthi M, et al. Prediction of normal bone anatomy for the planning of corrective osteotomies of malunited forearm bones using a three-dimensional statistical shape model. J Orthop Res 2017;35:2630–6. doi:10.1002/jor.23576.
[18] Plessers K, Vanden Berghe P, Van Dijck C, Wirix-Speetjens R, Debeer P, Jonkers I, et al. Virtual reconstruction of glenoid bone defects using a statistical shape model. J Shoulder Elb Surg 2017;27:160–6. doi:10.1016/j.jse.2017.07.026.
[19] Zhang J, Besier TF. Accuracy of femur reconstruction from sparse geometric data using a statistical shape model. Comput Methods Biomech Biomed Engin 2017;20:566–76. doi:10.1080/10255842.2016.1263301.
[20] Schumann S, Bieck R, Bader R, Heverhagen J, Nolte LP, Zheng G. Radiographic reconstruction of lower-extremity bone fragments: a first trial. Int J Comput Assist Radiol Surg 2016;11:2241–51. doi:10.1007/s11548-016-1427-y.
[21] van Lenthe GH, de Waal Malefijt MC, Huiskes R. Stress shielding after total knee replacement may cause bone resorption in the distal femur. J Bone Jt Surg 1997;79:117–22. doi:10.1302/0301-620X.79B1.6808.
[22] Huiskes R, Weinans H, Rietbergen B van. The relationship between stress shielding and bone resorption around total hip stems and the effects of flexible materials. Clin Orthop Relat Res 1992 NA; 124–134. doi:10.1097/00003086-199201000-00014.
[23] Goodship AE, Watkins PE, Rigby HS, Kenwright J. The role of fixator frame stiffness in the control of fracture healing. An experimental study. J Biomech 1993;26:1027–35.
[24] Claes L, Augat P, Suger G, Wilke HJ. Influence of size and stability of the osteotomy gap on the success of fracture healing. J Orthop Res 1997;15:577–84. doi:10.1002/jor.1100150414.
[25] Epari DR, Kassi J-P, Schell H, Duda GN. Timely fracture-healing requires optimization of axial fixation stability. J Bone Joint Surg Am 2007;89:1575–85. doi:10.2106/JBJS.F.00247.
[26] Bah MT, Shi J, Browne M, Suchier Y, Lefebvre F, Young P, et al. Exploring inter-subject anatomic variability using a population of patient-specific femurs and a statistical shape and intensity model. Med Eng Phys 2015;37:995–1007. doi:10.1016/j.medengphy.2015.08.004.
[27] Bryan R, Mohan PS, Hopkins A, Galloway F, Taylor M, Nair PB. Statistical modelling of the whole human femur incorporating geometric and material properties. Med Eng Phys 2010;32:57–65. doi:10.1016/j.medengphy.2009.10.008.
[28] Grassi L, Väänänen SP, Ristinmaa M, Jurvelin JS, Isaksson H. Prediction of femoral strength using 3D finite element models reconstructed from DXA images: validation against experiments. Biomech Model Mechanobiol 2017;16:989–1000. doi:10.1007/s10237-016-0866-2.
[29] Zhang J, Hislop-Jambrich J, Besier TF. Predictive statistical models of baseline variations in 3-D femoral cortex morphology. Med Eng Phys 2016;38:450–7. doi:10.1016/j.medengphy.2016.02.003.
[30] Park JS, Chung MS, Hwang SB, Shin BS, Park HS. Visible Korean human: its techniques and applications. Clin Anat 2006;19:216–24. doi:10.1002/ca.20275.
[31] Nolte D, Tsang CK, Zhang KY, Ding Z, Kedgley AE, Bull AMJ. Non-linear scaling of a musculoskeletal model of the lower limb using statistical shape models. J Biomech 2016;49:3576–81. doi:10.1016/j.jbiomech.2016.09.005.
[32] Rueckert D, Sonoda LI, Hayes C, Hill DLG, Leach MO, Hawkes DJ. Nonrigid registration using free-form deformations : application to breast MR images. IEEE Trans Med Imaging 1999;18:712–21. doi:10.1109/42.796284.
[33] Shontz SM, Vavasis SA. Analysis of and workarounds for element reversal for a finite element-based algorithm for warping triangular and tetrahedral meshes. BIT Numer Math 2010;50:863–84. doi:10.1007/s10543-010-0283-3.
[34] Cootes TF, Taylor CJ, Cooper DH, Graham J. Active shape models-their training and application. Computer Vision and Image Understanding 1995;61(1):38–59. doi:10.1006/cviu.1995.1004.
[35] Besl P, McKay N. A method for registration of 3-d shapes. IEEE Trans Pattern Anal Mach Intell 1992;14:239–56. doi:10.1109/34.121791.
[36] Powell MJD. A direct search optimization method that models the objective and constraint functions by linear interpolation. Advances in Optimization and Numerical Analysis. DordrechtNetherlands: Springer; 1994. p. 51–67. doi:101007/978-94-015-8330-5_4.
[37] Storn R, Price K. Differential evolution – a simple and efficient heuristic for global optimization over continuous spaces. J Glob Optim 1997;11:341–59. doi:10.1023/A:1008202821328.
[38] Kobyliansky E, Weissman SL, Nathan H. Femoral and tibial torsion – a correlation study in dry bones. Int Orthop 1979;3:145–7. doi:10.1007/BF00266885.
[39] Murphy SB, Simon SR, Kijewski PK, Wilkinson RH, Griscom NT. Femoral anteversion. J Bone Joint Surg Am 1987;69:1169–76. doi:10.1097/01241398-198707000-00026.
[40] Ding Z, Nolte D, Kit Tsang C, Cleather DJ, Kedgley AE, Bull AMJ. In vivo knee contact force prediction using patient-specific musculoskeletal geometry in a segment-based computational model. J Biomech Eng 2016;138:021018. doi:10.1115/1.4032412.

[41] Cleather DJ, Bull AMJ. The development of a segment-based musculoskeletal model of the lower limb: introducing FREEBODY. R Soc Open Sci 2015;2:140449. doi:10.1098/rsos.140449.
[42] Wu G, Siegler S, Allard P, Kirtley C, Leardini A, Rosenbaum D, et al. ISB recommendation on definitions of joint coordinate system of various joints for the reporting of human joint motion—part I: ankle, hip, and spine. J Biomech 2002;35:543–8. doi:10.1016/S0021-9290(01)00222-6.
[43] Mueller DK, Kutscherenko A, Bartel H, Vlassenbroek A, Ourednicek P, Erckenbrecht J. Phantom-less QCT BMD system as screening tool for osteoporosis without additional radiation. Eur J Radiol 2011;79:375–81. doi:10.1016/j.ejrad.2010.02.008.
[44] Taddei F, Schileo E, Helgason B, Cristofolini L, Viceconti M. The material mapping strategy influences the accuracy of CT-based finite element models of bones: an evaluation against experimental measurements. Med Eng Phys 2007;29:973–9. doi:10.1016/j.medengphy.2006.10.014.
[45] Schileo E, Dall'Ara E, Taddei F, Malandrino A, Schotkamp T, Baleani M, et al. An accurate estimation of bone density improves the accuracy of subject-specific finite element models. J Biomech 2008;41:2483–91. doi:10.1016/j.jbiomech.2008.05.017.
[46] Morgan EF, Bayraktar HH, Keaveny TM. Trabecular bone modulus-density relationships depend on anatomic site. J Biomech 2003;36:897–904. doi:10.1016/S0021-9290(03)00071-X.
[47] Świątek-Najwer E, Otto K, Krowicki P, Krysztoforski K, Keppler P, Kozak J. 3D bone shape modelling basing on dataset recorded by ultrasound free-hand navigated probe, 2014, p. 45–56. doi:10.1007/978-3-319-06596-0_5.
[48] Barratt DC, Chan CSK, Edwards PJ, Penney GP, Slomczykowski M, Carter TJ, et al. Instantiation and registration of statistical shape models of the femur and pelvis using 3D ultrasound imaging. Med Image Anal 2008;12:358–74. doi:10.1016/j.media.2007.12.006.
[49] Yadav P, Shefelbine SJ, Gutierrez-Farewik EM. Effect of growth plate geometry and growth direction on prediction of proximal femoral morphology. J Biomech 2016;49:1613–19. doi:10.1016/j.jbiomech.2016.03.039.
[50] Hartel MJ, Petersik A, Schmidt A, Kendoff D, Nüchtern J, Rueger JM, et al. Determination of femoral neck angle and torsion angle utilizing a novel three-dimensional modeling and analytical technology based on CT datasets. PLoS One 2016;11:1–10. doi:10.1371/journal.pone.0149480.
[51] Cibulka MT. Determination and significance of femoral neck anteversion. Phys Ther 2004;84:550–8. doi:10.1093/ptj/84.6.550.
[52] Takai S, Sakakida K, Yamashita F, Suzu F, Izuta F. Rotational alignment of the lower limb in osteoarthritis of the knee. Int Orthop 1985;9:209–15.
[53] Burghardt RD, Paley D, Specht SC, Herzenberg JE. The effect on mechanical axis deviation of femoral lengthening with an intramedullary telescopic nail. J Bone Jt Surg Br 2012;9494:1241–5. doi:10.1302/0301-620X.94B9.
[54] Speirs AD, Heller MO, Duda GN, Taylor WR. Physiologically based boundary conditions in finite element modelling. J Biomech 2007;40:2318–23. doi:10.1016/j.jbiomech.2006.10.038.
[55] Duda GN, Heller M, Albinger J, Schulz O, Schneider E, Claes L. Influence of muscle forces on femoral strain distribution. J Biomech 1998;31:841–6. doi:10.1016/S0021-9290(98)00080-3.
[56] Zhang QH, Cossey A, Tong J. Stress shielding in periprosthetic bone following a total knee replacement: effects of implant material, design and alignment. Med Eng Phys 2016;38:1481–8. doi:10.1016/j.medengphy.2016.09.018.
[57] Väänänen SP, Grassi L, Flivik G, Jurvelin JS, Isaksson H. Generation of 3D shape, density, cortical thickness and finite element mesh of proximal femur from a DXA image. Med Image Anal 2015;24:125–34. doi:10.1016/j.media.2015.06.001.
[58] Keating JF, Simpson AHRW, Robinson CM. The management of fractures with bone loss. J Bone Joint Surg Br 2005;87B:142–50. doi:10.1302/0301-620x.87b2.15874.
[59] Pierre MA, Zurakowski D, Nazarian A, Hauser-Kara DA, Snyder BD. Assessment of the bilateral asymmetry of human femurs based on physical, densitometric, and structural rigidity characteristics. J Biomech 2010;43:2228–36. doi:10.1016/j.jbiomech.2010.02.032.